Water Research 165 (2019) 114971

Contents lists available at ScienceDirect

Water Research

journal homepage: www.elsevier.com/locate/watres

High-fidelity profiling and modeling of heterogeneity in wastewater systems using milli-electrode array (MEA): Toward high-efficiency and energy-saving operation

Zhiheng Xu [a], Farzaneh MahmoodPoor Dehkordy [a], Yan Li [b], Yingzheng Fan [a], Tianbao Wang [a], Yuankai Huang [a], Wangchi Zhou [a], Qiuchen Dong [c], Yu Lei [c], Matthew D. Stuber [c], Amvrossios Bagtzoglou [a], Baikun Li [a, *]

[a] Department of Civil & Environmental Engineering, University of Connecticut, Storrs, Connecticut 06269, United States
[b] Department of Environmental Engineering, Jilin University, Changchun, Jilin Province, 130022, China
[c] Department of Chemical and Biomolecular Engineering, University of Connecticut, Storrs, Connecticut 06269, United States

ARTICLE INFO

Article history:
Received 20 February 2019
Received in revised form
8 August 2019
Accepted 9 August 2019
Available online 10 August 2019

Keywords:
High-fidelity profiling
Milli-electrode array (MEA)
Wastewater treatment
Real time *in situ* monitoring
Navier-Stokes equations
Energy-saving and performance enhancement

ABSTRACT

High energy consumption is a critical problem for wastewater treatment systems currently monitored using conventional “single point” probes and operated with manual or automatic open-loop control strategies, exhibiting significant time lag. This challenge is addressed in this study by profiling the variation of three critical water quality parameters (conductivity, temperature and pH) along the depth of a reactor at high spatiotemporal resolution in a real-time mode using flat thin milli-electrode array (MEA) sensors. The profiling accurately captured the heterogeneous status of the reactor under transient shocks (conductivity and pH) and slow lingering shock (temperature), providing an effective dataset to optimize the chemical dosage and energy requirement of wastewater treatment systems. Transient shock models were developed to validate the MEA profiles and calculate mass transfer coefficients. Monte Carlo simulation revealed high-resolution MEA profiling combined with fast closed-loop control strategies can save 59.50% of energy consumption (Temperature and oxygen consumption controls) and 45.29% of chemical dosage, and reach 16.28% performance improvement over the benchmark (defined with ideal conditions), compared with traditional “single-point” sensors that could only monitor the entire system through a single process state. This study demonstrated the capability of MEA sensors to profile reactor heterogeneity, visualize the variation of water quality at high resolution, provide complete datasets for accurate control, and ultimately lead to energy-saving operation with high resilience.

1. Introduction

High energy consumption and low treatment performance are two critical problems for wastewater treatment systems currently monitored using conventional “single point” probes and operated with manual or automatic open-loop control approaches. Vigorous mixing of oxygen and biomass within wastewater generates a heterogeneous environment where contaminant concentration varies along the depth and length of treatment systems (Chang et al., 2002; Le-Clech et al., 2006; Xu et al., 2012; Schaider et al., 2017). However, existing “single-point” probes can only measure single process parameters or states (e.g., pH, redox potential, and oxygen) without capturing a complete picture of the heterogeneity within systems. Determining wastewater quality parameters (e.g., chemical oxygen demand (COD), nitrogen, phosphonate and free chlorine) has historically required tedious sampling and off-site analysis (Dewettinck et al., 2001; Beltrá et al., 2003; Nowack, 2003; Jin et al., 2004; Pehlivanoglu-Mantas and Sedlak, 2008; Yu et al., 2009), with operation normally executed empirically without knowing the *in situ* physiochemical status, leading to fluctuating effluent quality and high operational cost (e.g., over-aeration and over-chemical dosage)(Xianghua and Jun 2009; Yang et al., 2010). Water quality monitoring technologies should be innovated to capture the “local” abnormality (e.g., irregular effluent concentration, pH sudden drop, mixing dead-zone, etc.) at an early stage to enable effective feedback control, enhance system

---

* Corresponding author.
E-mail address: baikun.li@uconn.edu (B. Li).

https://doi.org/10.1016/j.watres.2019.114971
0043-1354/

robustness and treatment performance, and reduce energy consumption.

Enormous efforts have been conducted for real-time decoding of the "black box" of wastewater systems. Multiparameter meters (e.g. Hach®, YSI®) integrating multiple probes into a single cartridge have been widely used. However, these types of sensors not only occupy a large space (diameter: 0.4 m; length: 1–1.5 m), but they are costly ($25,000-$50,000 per meter) due to complicated sensor materials, waterproof layers, anti-biofouling layers, data transfer and electronic units, and development- and commercialization-related costs (Linsenmeier and Yancey, 1987). Such a high cost and large space requirement make mass deployment of such sensors along the depth and length of wastewater systems infeasible. Furthermore, current monitoring technologies only utilize single-point probes to monitor only one point of the entire systems (Dewettinck et al., 2001; Beltrá et al., 2003; Nowack, 2003; Jin et al., 2004; Pehlivanoglu-Mantas and Sedlak, 2008; Yu et al., 2009). Therefore, cost-beneficial easy-to-deploy sensor arrays should be developed for profiling multiple parameters at multiple points for capturing the dynamic heterogeneous states of the system. Microelectrodes have been developed in last two decades, especially the micro-scale glass pipette electrodes (Bishop and Yu, 1999; Lee et al., 2007; Korostynska et al., 2012). However, the fragile glass pipette structure, time-consuming fabrication, and the need for bulky micromanipulators to position microelectrodes have posed severe problems for field application (Jensen et al., 2011; Krause et al., 2013; Xu et al., 2016, 2017). Recently developed milli-electrodes fabricated by photolithography with chemical vapor deposition (PCVD) have been limited by the strict fabrication conditions, deployment difficulty in wastewater treatment systems, and high cost photomask and metal deposition in PCVD protocols (Lee and Lee, 2003; Lee et al., 2008; Yan et al., 2011). Flat thin mm-sized electrochemical sensors are expected to tackle this challenge (Kinlen et al., 1994; Hahn et al., 1995; Marzouk et al., 1998; Ges et al., 2007; Ibanez and Zamborini, 2008). Milli-electrode arrays (MEAs) consisting of multiple types of mm-sized sensors (e.g., pH, temperature, oxygen, conductivity, hypochlorite and chloride) have been developed using inkjet printing technology (IPT) (Xu et al., 2016, 2017), in which metallic inks (e.g., gold, silver) are precisely printed on a flat flexible material (e.g., polyimide film). Multiple rows of sensors can be aligned using IPT for profiling wastewater systems at high spatiotemporal resolution, which can capture heterogeneity throughout the entire reactor. It could fundamentally transform the state-of-the-art real-time wastewater monitoring methodology. In addition, these miniature-sized electrodes possess distinct advantages over traditional large electrodes, including compact structure, addressable multiple types of sensors, and minimal intrusion to biochemical systems.

Finite-element simulations have become a powerful tool to elucidate the heterogeneous state of wastewater systems (Grilli et al., 2013; Dickinson et al., 2014; Odu et al., 2016; Adadevoh et al., 2017; Huang et al., 2018). COMSOL Multiphysics (COMSOL, Inc, Burlington, MA, USA) has been widely used for finite-element simulation and has the capability to simulate the incorporation and coupling of diverse physical phenomena within one model (Grilli et al., 2013; Dickinson et al., 2014; Odu et al., 2016; Adadevoh et al., 2017; Huang et al., 2018). The desired phenomena often originate from traditionally separate fields of applied physics and engineering. To investigate the heterogeneous states of wastewater systems, a study involving fluid dynamics, mass transport, heat transfer, and charge transfer is necessary (Grilli et al., 2013; Dickinson et al., 2014; Odu et al., 2016; Adadevoh et al., 2017; Huang et al., 2018). Multiphysics simulations can provide physical insight and predict concentration or temperature profiles by capturing accurately the relevant phenomena.

The breakthrough of this study lies in high-fidelity profiling of the heterogeneity in a reactor using a series of MEA sensors and validated by numerical finite element simulations in COMSOL Multiphysics, through which the fluctuation of water quality can be readily visualized in a spatiotemporal fashion. There are three major tasks in this study. First, the variation of three water quality parameters (conductivity, temperature, and pH) along the depth of a reactor was profiled using MEA sensors under steady state and transient shocks. Second, the heterogeneity of two physical parameters (conductivity and temperature) in the reactor was validated by COMSOL Multiphysics simulations of multiple physical phenomena. Finally, energy savings, chemical savings, and treatment performance as the result of high-resolution MEA profiling, were estimated using Monte Carlo simulation and compared side-by-side with traditional "single-point" sensing technology.

2. Materials and methods

2.1. Three types of MEA sensors

Three important water quality parameters: conductivity (Levlin, 2010), temperature (Ahsan et al., 2005), and pH (SYSTEMS) were targeted in this study. All types of MEA sensors (each size: 2 cm × 0.5 cm) were precisely printed on a Kapton FPC polyimide film (thickness: 127 μm, American Durafilm) by a Dimatix Materials Printer (ModelDMP-2800, FUJIFILM Dimatix, Inc.) as previously described (Fig. 1a) (Xu et al., 2016, 2017). The signal output of the conductivity and temperature MEAs is electrical resistance in units of milliohm, while the signal output of the pH MEAs is electrical potential in units of millivolts.

2.2. Experiment setup

The batch-mode reactor was a plastic cylinder with a diameter of 62 mm and a height of 180 mm. The reactor's heterogeneous state was profiled in real-time using three of each type of MEA sensors clipped by 3D-printed holders on three locations along the depth of the reactor (Fig. 1b and 1c) (top location: 40 mm below the water surface, middle location: 85 mm below the water surface, and deep location: 130 mm below the water surface). Since the location of the shock injection could affect mass transfer and

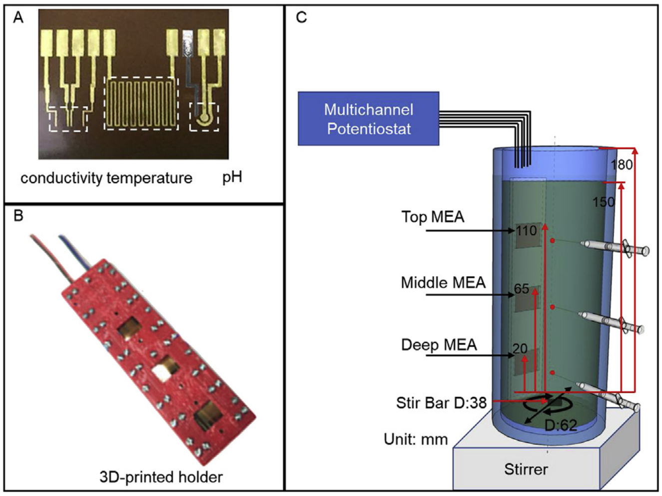

Fig. 1. The experimental setup for profiling tests. (A: MEA film consisting of conductivity sensor, temperature sensor, and pH sensor. B: MEA in a 3D printed holder to put inside the reactor. C: the diagram of shock test in the beaker (The unit of the dimension is in millimeter.).

chemical profiles along the reactor depth, the injection points were positioned at the same depth as the three holders (Fig. 1) to assure the accurate injection point of shock solutions (conductivity and pH), while temperature shock was introduced only through heating the bottom surface of the reactor (Fig. 1c). Before the shock tests, the solution in the reactor was well-mixed and the readings of each MEA sensor were recorded using a multi-channel potentiostat (1040C 8-channel potentiostat, CH Instruments, Inc.) every 2 s for over 10 min. For each shock test, the transient shock was injected individually into one of the three locations (top, middle and deep) using a syringe located at the same height of the MEA sensors. The water solution in the reactor was continuously stirred using a cubic stirring bar (size: 38 × 6.5 × 6.5 mm) on the bottom of the reactor, with a rotation rate of 50 RPM for conductivity, temperature, and pH shock experiments and at 200 RPM for additional conductivity and temperature shock experiments.

2.3. MEA profiling along the depth of a reactor under shocks

For conductivity shocks, 200 μL (100 g/L) sodium chloride (NaCl, Fisher Science, Co.) was injected into the reactor with the initial solution of 380 mL sodium chloride (2 mg/L NaCl). The initial conductivity of the solution was measured as 4.42 ± 0.22 μS/cm using a commercial conductivity sensor (Thermo Scientific Orion 3-star conductivity meter). For pH shock, 200 μL of 1 M potassium hydroxide solution (KOH, Fisher Science, Co.) mixed in 2 mg/L NaCl solution (pH: 14) was injected into the reactor with the initial pH of 7.22 (380 mL NaCl (2 mg/L) solution). The pH of the water solution was validated using a commercial pH sensor (Thermo Scientific Orion 3-star pH meter). For temperature shock, the heating source was a heating plate located at the bottom of the reactor with the initial temperature of the water solution of 18.5 ± 0.12 °C (room temperature). The temperature of the water solution was measured using a commercial temperature sensor (Thermo Scientific Orion 3-star conductivity meter). The heating plate surface temperature increased from room temperature to 200 °C within 30 s, and then dropped gradually to room temperature over 12 min (Fig. S1). All shock tests were conducted in triplicate.

2.4. Model development and validation

Numerical finite element models were developed in COMSOL Multiphysics (COMSOL, Inc, Burlington, MA, USA) to validate the aforementioned MEA profiles. Flow in the reactor was modeled by the Navier-Stokes equations using the Arbitrary Lagrangian-Eulerian (ALE) technique (Hughes et al., 1981; Duarte et al., 2004) (Eq. (1) and Eq. (2)):

$$\frac{\partial \rho}{\partial t} - \frac{\partial \boldsymbol{x}}{\partial t}\cdot\nabla\rho + \nabla\cdot(\rho\boldsymbol{u}) = 0 \tag{1}$$

$$\rho\left(\frac{\partial \boldsymbol{u}}{\partial t} - \frac{\partial \boldsymbol{x}}{\partial t}\cdot\nabla\boldsymbol{u}\right) + \rho(\boldsymbol{u}\cdot\nabla)\boldsymbol{u} = \nabla\cdot[-p\mathbf{I} + \tau] + \boldsymbol{F} \tag{2}$$

Here, ρ is density, $\boldsymbol{u} = \boldsymbol{v} + \frac{\partial \boldsymbol{r}}{\partial t}$, where $\boldsymbol{v}$ is the velocity vector in the rotating coordinate system, and $\boldsymbol{r}$ is the position vector, t is the mesh reference time, $\boldsymbol{x}$ is a function of angular velocity and time, p is pressure, τ is shear stress, and $\boldsymbol{F}$ is the external force vector. To simulate the flow in the reactor, a fixed domain and a rotating domain were defined and coupled using a continuity boundary condition on the common interior walls. No-slip boundary conditions were imposed at the exterior walls of the reactor representing no fluid velocity at the solid walls of the reactor. Additionally, a zero-shear stress condition was assumed on the top boundary. The flow field was modeled by the frozen rotor assumption, a special case of steady state, to avoid computationally expensive simulations.

2.5. Monte Carlo simulation of energy-saving and treatment performance improvement in treatment systems using high-resolution MEA profiling

Monte Carlo simulation was used to simulate energy savings, chemical dose savings, and treatment performance improvement with high-resolution MEA profiling and accurate feedback control (Mooney, 1997; Williams and Ebel, 2014). Three targeted parameters (temperature, conductivity, and pH) were assumed to vary steadily throughout the length of a plug-flow reactor (PFR) (with an aerobic nitrification tank as the example in this study). In contrast, the homogeneity of ideal completely stirred tank reactors (CSTR) would lead to the identical readings of all MEA sensors deployed along the reactors. Existing "single-point" sensors can only monitor the worst-case scenario in order to meet the requirement of effluent water quality, and consequently cause energy overconsumption, chemical overuse and low treatment performance for the areas without monitoring. Thereby, Monte Carlo simulation was used to predict the heterogeneity of these three parameters measured by multiple units of MEA sensors along PFR. In the Monte Carlo simulation, the "single-point" sensor would be positioned at the beginning section or the end section of the plug-flow reactor, while multiple MEA sensors (eight MEA units of each type were assumed in this study) would be positioned uniformly along the length of the tank and connected to the air supply (for aeration) and chemical pump (for dosage) controlled in a real-time mode. Two assumptions were made to simplify Monte Carlo simulation. First, biochemical reactions (e.g., COD removal, nitrification) progress uniformly along the length of the PFR, so that these three parameters (temperature, conductivity, and pH) would change linearly along the reactor. Second, these three parameters would be sampled from a uniform distribution in each zone monitored by MEAs. The energy savings was calculated from the Monte Carlo simulation of temperature and conductivity, the chemical dosage savings was calculated from the Monte Carlo simulation of pH, and treatment performance was calculated by simplifying the relationship between temperature and biologic reactions. The optimum temperature for biochemical reactions in wastewater is 30 °C, at which treatment performance is defined as 100% and declines with both higher and lower operating temperatures than the optimum. The Monte-Carlo simulation was performed with 10,000 iterations.

3. Results and discussion

3.1. MEA profiling of conductivity under transient shocks

The initial conductivity of the solution (2 mg/L NaCl) in the reactor was 4.42 ± 0.22 μS/cm. With the shock solution (2 μL NaCl solution, 100 g/L) being injected at the top location (40 mm below the water surface) on the 60th second after reaching steady state, the conductivity increased rapidly in the first 35 s after the shock (Table 1). The peak value of the conductivities at the top, middle, and deep positions of the reactor were 318.33 ± 8.19 μS/cm, 68.82 ± 1.45 μS/cm, and 88.52 ± 2.03 μS/cm, respectively, indicating that the top MEA increased fastest as it was the closest to the shock injection (Fig. 2a). The peak value of the middle MEA being lower than that of the deep MEA can be explained by the slow mass transfer in the possible dead zone within the middle section. The stirring bar on the bottom of the reactor caused more vigorous mixing within the deep section than in the middle section (Huang et al., 2018), leading to the shortcut of mass transfer from the top

Table 1
Response time of the conductivity, temperature and pH MEA sensors under the shocks on the top, middle and deep locations. (Response time layout (sec.): Total response time/Time from steady state to peak/Time from peak to steady state. NA: Not available since the peak was not detected throughout the process.).

		Top sensor	Middle sensor	Deep sensor
Conductivity-50 rpm	**Top shock**	178/36/142	216/16/200	216/20/196
	Middle shock	216/NA/NA	224/36/188	216/NA/NA
	Deep shock	220/NA/NA	182/34/148	182/34/148
Conductivity-200 rpm	**Top shock**	25/5/20	25/NA/NA	25/NA/NA
	Middle shock	20/NA/NA	20/5/15	20/NA/NA
	Deep shock	25/NA/NA	25/5/20	25/5/20
Temperature -50 rpm		540	540	540
Temperature -200 rpm		540	540	540
pH-50 rpm	**Top shock**	40/8/32	40/12/28	40/16/24
	Middle shock	82/22/60	82/8/74	82/12/70
	Deep shock	38/32/6/38	82/8/74	38/8/30

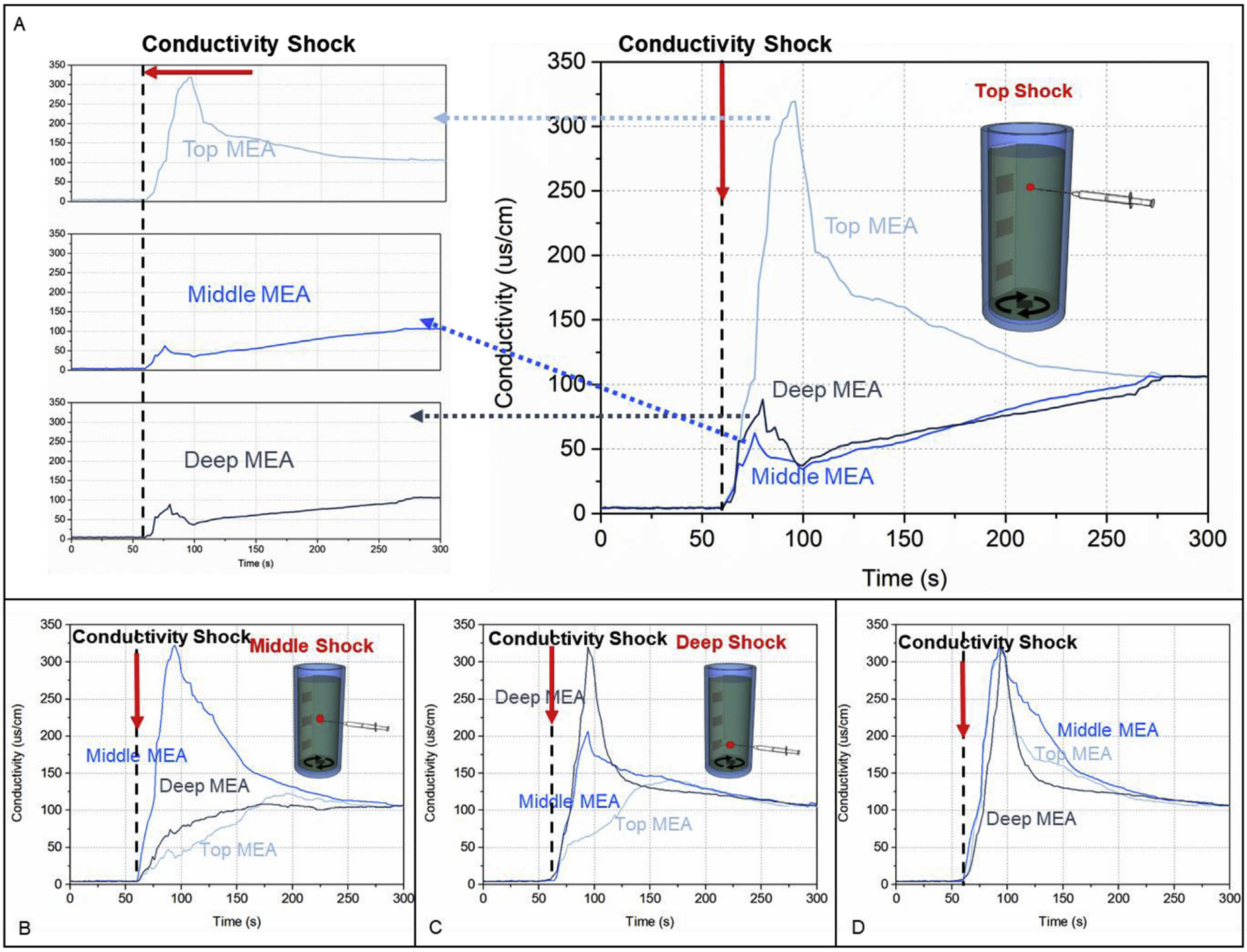

Fig. 2. Heterogeneity profiling of conductivity under transient shocks at top/middle/deep locations occurring at the 60th second with the mixing rate of 50 RPM. (A: Three conductivity MEAs responses after the top-position shock; B: Three conductivity MEAs responses after the middle-position shock; C: Three conductivity MEAs responses after the deep-position shock; D: The top MEA response after the top-position shock, the middle MEA response after the middle-position shock, and the deep MEA response after the deep-position shock.)

section to the deep section and the lower mass transfer to the middle section. The conductivity of the top MEA dropped gradually over 190 s to the steady state conductivity of 106.11 ± 2.55 μS/cm, while the conductivity readings of the middle and deep MEA dropped gradually in 20 s and then slowly increased to the steady state conductivity of 106.11 ± 2.55 μS/cm. With the shock solution (2 μL NaCl solution, 100 g/L) being injected at the middle location (85 mm below the water surface), the conductivity peak value of the middle MEA was highest among the three MEAs (Fig. 2b), demonstrating that the injection location influences the diffusion pattern of Na^+ and Cl^- ions in the reactor. It should be noted that the conductivity reading of the deep MEA was slightly higher than that of the top MEA in the first 170 s post-injection, which was caused by faster mass transfer from more vigorous mixing in the deep section than in the top section, since the stirring bar was located on the bottom of the reactor. The results of the shock injection at the deep location (Fig. 2c) confirmed that the shock location and the stirring bar location are two key factors for the observed transient conductivity profiles (Fig. S2A).

The conductivity readings of the top MEA under top shock, the middle MEA under middle shock, and the deep MEA under deep shock reached the maximum value of ~318 μS/cm and then dropped sharply to the final value of ~106 μS/cm (Fig. 2d), indicating that NaCl diffusion occurred similarly near the shock injection location even at the slow mixing rate (50 rpm). It should be noted that the peak for the middle MEA was much wider than the top and deep MEAs (Fig. 2d), which corresponded well with its relatively slow response time after the peak (Table 1) and supports the claim that the middle section had the lowest rate of mass transfer. In contrast, the response time of MEA sensors was similar for all three shocks at the high mixing rate (200 rpm) (Fig. S3), demonstrating that the difference of diffusion rate among these three-position shocks declined with mixing intensity, as the result of faster mass transfer under a higher mixing rate.

With the initial concentration of NaCl solution as 2 mg/L and the shock concentration of NaCl solution as 100 g/L, the final concentration of the bulk NaCl solution should be 54.60 mg/L and the theoretical conductivity should be around 105 μS/cm, which matched well with the bulk solution conductivity (106 μS/cm) measured by the commercial conductivity sensor and the stable readings of three conductivity MEAs 220 s after the shock tests (Fig. 2).

The heterogeneous conductivities measured by MEAs were validated using an electrical conductivity (EC) model simulation that mainly includes two partial differential equations (PDEs) consisting of mass transport and fluid dynamics (Fig. S4). According to the fluid dynamics simulation, the particle movement (water molecule with Na^+ and Cl^- ions, 0.04–0.08 m/s) within the deep location was much faster than (0.01 m/s) within the top location (Fig. S4). Examples of the streamlines and NaCl concentration isosurfaces for one snapshot in time ($t = 2.5s$) are shown in Fig. S4. Furthermore, the comparison between experimental and simulation results for EC heterogeneity was conducted in dimensionless form (Fig. 3a–c), since the release volume and the rate of release of the NaCl shock was difficult to be standardized and thus impossible to be faithfully reproduced in the simulation. The simulation and experimental results followed the same trend for the conductivity MEA closest to the shock location (e.g., top MEA under top shock, middle MEA under middle shock, and deep MEA under deep shock) (Fig. 3a–c). However, there was a large discrepancy between the CFD simulated result and the sensor profiles of middle MEA under the middle shock (Fig. 3b), which had the lowest mass transfer effectiveness. The possible reason was that CFD simulation only considered the ideal condition (e.g., smoothness of the reactor, well mixing), and neglected the slow mass transfer in the middle location. When the mixing rate was accelerated to 200 RPM, the mass transfer became much faster than that at 50 RPM based on the response time (Figs. 4A–1, 4B-1 4C-1 and Table 1), which was clearly visualized using the MEA profiling.

High-resolution MEA profiling provided sufficient datasets to determine the volumetric mass transfer coefficient in the reactor (De Figueiredo and Calderbank, 1979; Johnson et al., 1990). The profiling results and numerical data were fitted to the solution of the differential equation using linear regression on the semi-log transformed data, assuming that the exponential decay starts at the peak concentration (Garcia-Ochoa and Gomez, 1998):

$$\frac{C_L}{C^*} = 1 + \alpha\, e^{-KL^*t} \tag{3}$$

where C_L is the liquid-phase concentration at a given point in time, C^* is the fully-mixed concentration, k_L is the mass transfer coefficient, and α is an adjustable parameter for better fitting in the rising or falling limbs of the curves. By fitting the solution of the differential equation (Eq. (3)) to the data obtained from three shock locations, the mass transfer coefficient was estimated (Figs. 4A–2, B-2, C-2). The fitted k_L ranges from 0.02 to 0.23 s^{-1} for the experimental and numerical results discussed herein, which is in reasonable agreement with the results (mass transfer coefficients range between 0.015 and 0.04 s^{-1} and 0.3 to 0.7 s^{-1}) previously reported (Ogut and Hatch, 1988; Valverde et al., 2016) and thus validate the CFD model.

3.2. Heterogeneity MEA profiling of pH under transient shocks

pH adjustment in water and wastewater treatment systems has been normally conducted by adding acidic/basic chemicals and monitoring using single-point pH sensors (Al-Ghusain et al., 1994; Choi and Park, 2001; Wunderlin et al., 2012). This approach fails at capturing the transient sharp change along spatial dimensions of systems. In this study, the initial pH of the solution (0.2 mg/L NaCl) in the reactor was 7.22, and the pH of the shock solution (1 M KOH solution) was 14.0, so that the final pH of the mixed solution should be 10 based on static models. The final pH of the mixed solution measured by the pH MEAs was 10.24 ± 0.19, which was similar to the values (10.22 ± 0.02) measured by the commercial pH sensor.

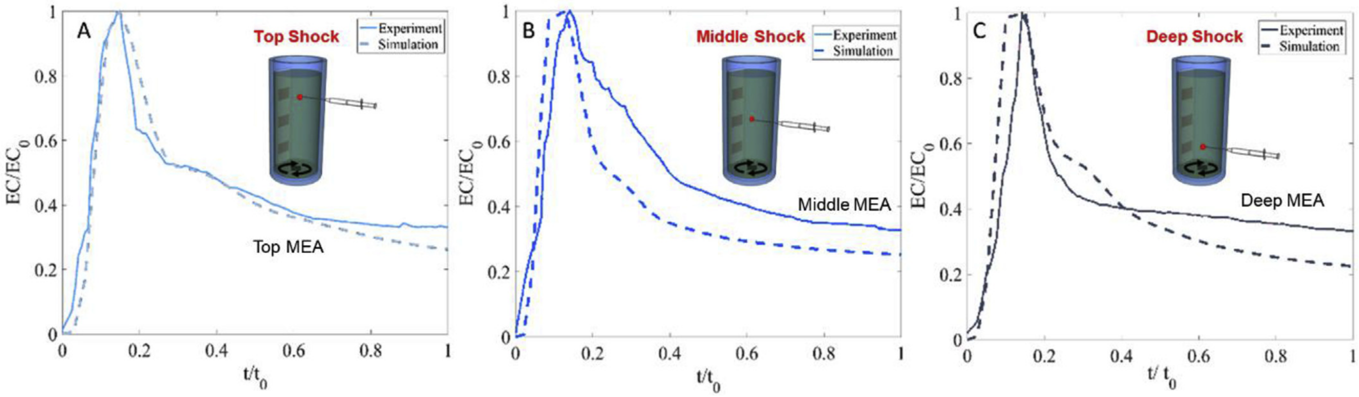

Fig. 3. Comparison between the conductivity experimental results (solid line) and fitted differential equation (dashed line) for the MEA sensors closest to the location of each shock at 50 RPM. (A. Top MEA after top shock. B. Middle MEA after middle shock C. Deep MEA after deep shock.)

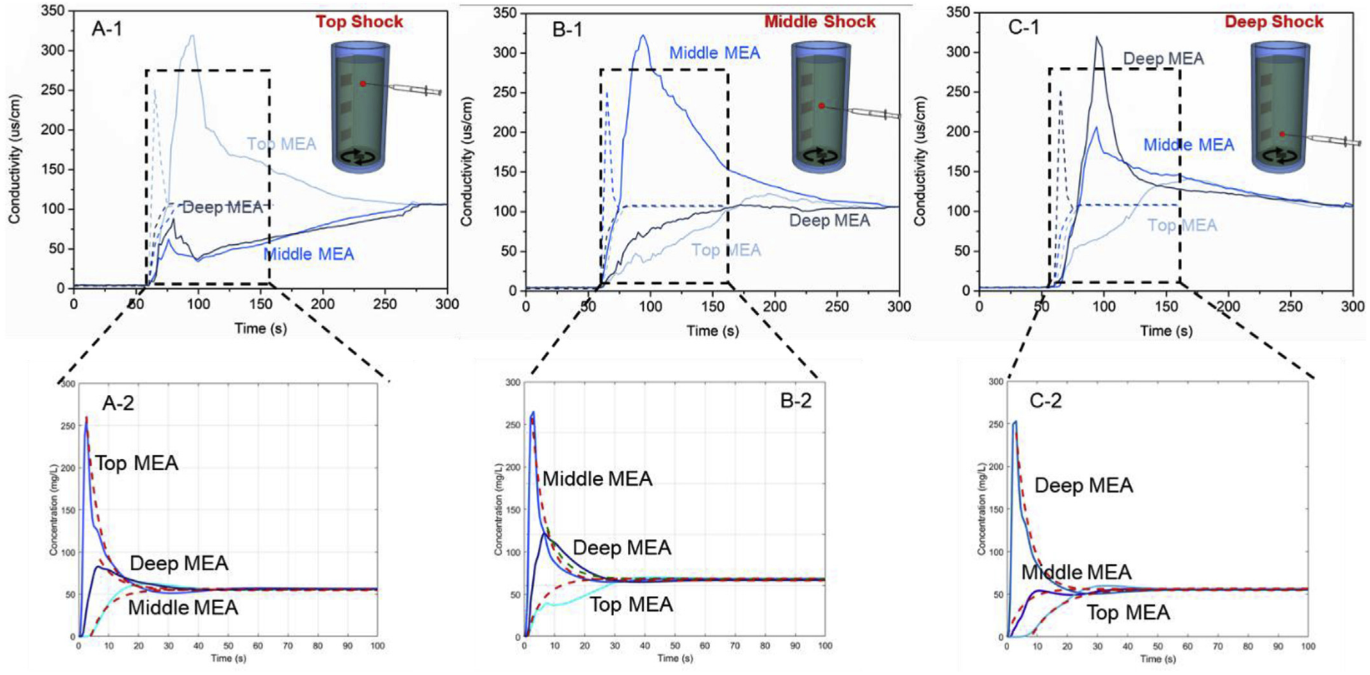

Fig. 4. The impact of mixing rates (50 RPM: solid line; 200 RPM: dashed line) on the heterogeneity profiling of conductivity under transient shocks occurring on the 60th second. (A: Three conductivity MEAs responses after the top-position shock; B: Three conductivity MEAs responses after the middle-position shock; C: Three conductivity MEAs responses after the deep-position shock.).

The behavior of pH and related phenomena are considered as the functions of time during the dynamic process (Ylén, 2001). The flow dynamics in the continuous flow process is described with partial material balances as:

$$\frac{d[A]}{dt} = \frac{1}{V}\left(F[A]_0 - F[\mathrm{A}]\right) \tag{4}$$

Where [A] is the concentration of ion A, t is the time, V is the volume of the reactor (378 mL), and F is flow rate of the ion, and $[A]_0$ is the ion A concentration of the influent. Due to the small volume of the pH shock solution (2 μL), the change in V can be neglected.

When 2 μL of KOH solution (1 M, pH:14) was injected at the top of the reactor, the pH reading of the top MEA increased promptly in the first 8 s, and then dropped gradually within 32 s to the steady-state pH of 10.24 ± 0.19. The maximum pH readings oat the top, middle and deep locations of the reactor were 13.80 ± 0.24, 11.51 ± 0.33, and 10.85 ± 0.34, respectively, indicating that pH decreased along the depth as the shock injection was near the top (Fig. 5a). This fits Jean's pH dynamic model of the strong base/strong acid (Ylén, 2001). The response of the middle MEA and deep MEA started on the 64th and 66th second, respectively, which was slower than that of the top MEA (60th second). This disparity is demonstrated by the flow dynamic equation (Eq. (4)), in which the distance between the sensors and the shock caused different response times (Table 1). In contrast, the response time of the middle and deep conductivity MEAs were not delayed in the conductivity profiles (Fig. 2a), which could be explained by different mass transfer patterns in the water solution (Fig. S1B). The mass transfer under conductivity shocks was mainly ion diffusion (Na^+ and Cl^-) driven by the mixing effect located on the bottom of the reactor, leading to the slowest mass transfer in the middle section (Fig. S2A). However, the mass transfer under pH shocks was correlated with ion diffusion as well as the bond of proton (H^+) with hydroxide ions (OH^-) (Ylén, 2001), which caused continuous mass transport between adjacent sections (Fig. S2B), leading to fast mass transfer and fast response of MEAs to the pH shock (Table 1). For the pH shock on the middle location, the pH reading of the middle MEA jumped to 13.80 ± 0.11 within the first 8 s and then gradually dropped to the pH of 10.24 ± 0.09 (Fig. 5b) at 74 s after the shock. During the whole shock test period, the pH of the middle MEA was always higher than that of the deep MEA, while the top MEA had the lowest pH value. The pH of the middle position increased faster than that on the top and deep locations due to short distance to the shock (the middle position). For the pH shock at the deep location, the deep MEA promptly captured the pH increase and the reading jumped faster than that at the top position due to the mixing effect (Fig. 5c).

The readings of the top MEA under top shock, the middle MEA under middle shock, and the deep MEA under deep shock jumped promptly to the maximum pH around 13.8 and then dropped gradually to the final pH of 10.22 (Fig. 5d). Corresponding to the longest duration from the peak pH to the final pH (Table 1), the middle MEA after middle shock exhibited the largest width of the peak (Fig. 5d), indicating that the middle section of the reactor had the slowest mixing effectiveness. Additionally, although the pattern of the pH profiles was similar to that of the conductivity profiles (Figs. 2a and 5a), the MEA sensors had much faster response to pH shocks than to conductivity shocks (30s vs. 220s) (Figs. 2d and 5d, Table 1), which was caused by the strong acid ionization reaction in the pH shock.

Besides promptly capturing the system heterogeneity under transient shocks, both conductivity and pH profiles revealed that MEA sensors could monitor the system homogeneity of uniform mixing in this batch-mode CSTR reactor before shock introduction (0–60 s) (Figs. 2a and 5a) and after the reactor recovered to equilibrium (after 250 s under conductivity shock, Fig. 2a; and after 140 s under pH shock, Fig. 5a). This well demonstrated the capability of high-resolution MEA profiling to validate the homogeneity of uniform complete mixing under steady status as well as capture the heterogeneity under transient shocks.

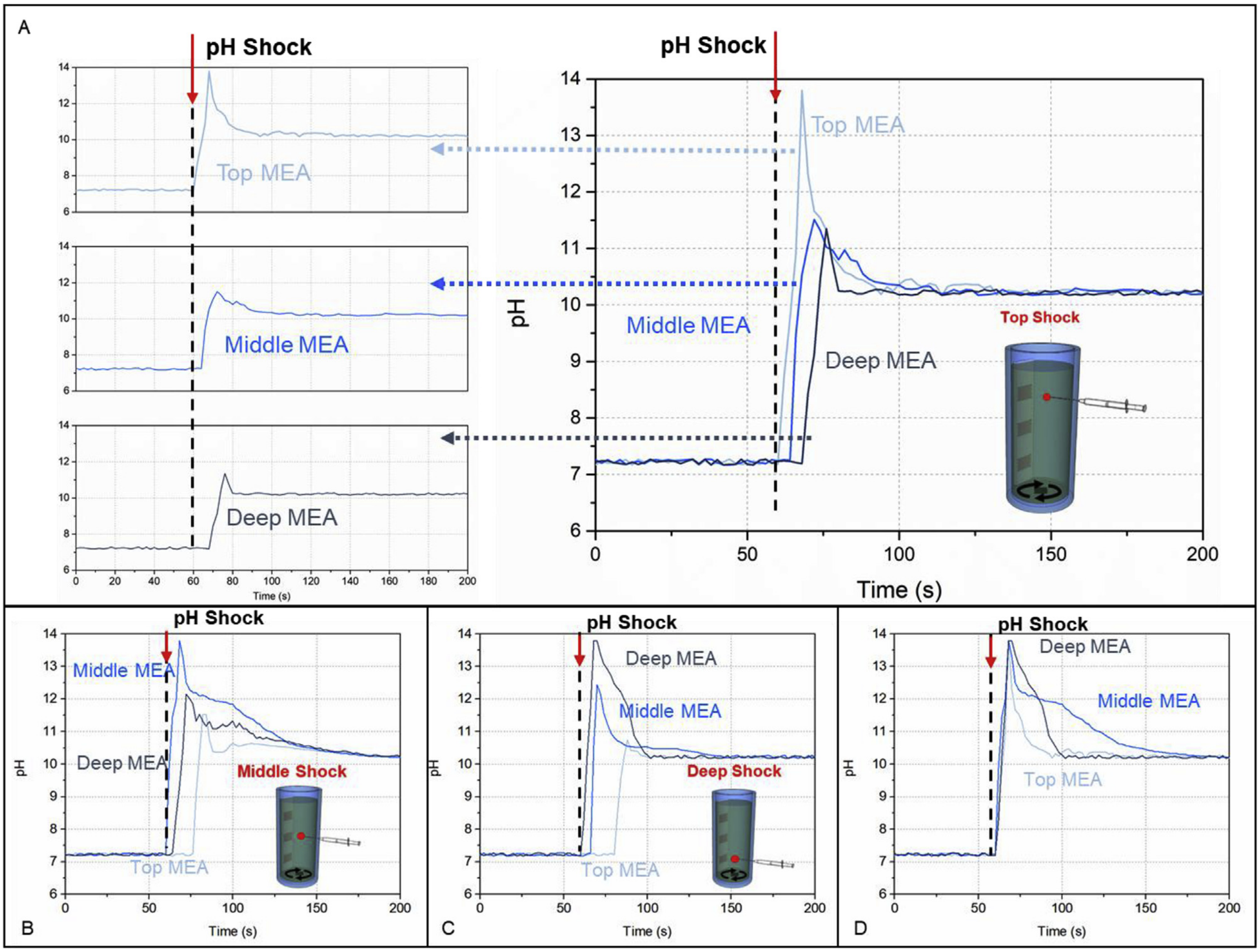

Fig. 5. Heterogeneity profiling of pH under transient shocks of top/middle/deep positions occurring at the 60th second with the mixing rate of 50 RPM. (A: Three pH MEAs responses after the top-position shock; B: Three pH MEAs responses after the middle-position shock; C: Three pH MEAs responses after the deep-position shock; D: The top MEA response after the top-position shock, the middle MEA response after the middle-position shock, and the deep MEA response after the deep-position shock.).

3.3. *Heterogeneity MEA profiling of temperature under slow lingering shock*

Temperature shock normally occurs when a spike of industrial wastewater (e.g., dairy farm, slaughterhouse) flows into municipal wastewater treatment plants (Borja and Banks, 1995; Massé and Masse, 2001; Ahsan et al., 2005). In this study, the initial steady-state temperature of the solution was 18.5 ± 0.12 °C throughout the well-mixed reactor. The temperature shock was introduced only at the bottom surface of the reactor through an external heating plate that gradually raised the temperature of the water solution for 30 s (Fig. 6a and Fig. S1), which was slower and lasted much longer than the conductivity shock and pH shock. The response pattern at fast mixing rate (200 RPM) was not substantially different from that at slow mixing rate (50 RPM, Table 1 and Fig. 6a and 6d). However, during the initial heating period (60s−300s), the temperature increase rate (0.017 °C/s) at 200 RPM was faster than that (0.014 °C/s) at 50 RPM, demonstrating that mixing intensity indeed affected heat transfer in the water solution. To compare the temperature heterogeneity profiling under this slow lingering temperature shock, a heat transfer simulation was performed with the initial temperature of 18.5 °C in the reactor. The flow profile used in this model was the same as the one used for the solute transport model, showing an excellent agreement between simulation and experimental results for all the three locations of temperature MEAs (Fig. 6b and 6c).

The temperature readings of three MEAs on the top, middle and deep locations of the reactor increased gradually to the final temperature (24.90 ± 0.18 °C, Fig. 6b), which matched well the readings of the commercial temperature sensor. Unlike the transient shocks of conductivity and pH instantaneously injected to a specific location along the depth of the reactor, the temperature shock was introduced steadily using the heating plate at the bottom of the reactor (Fig. S1), through which the heat transferred slowly from the bottom to the top of the whole reactor and the temperature profiles did not exhibit sharp peaks at any moment.

Because the temperature of the external heater was always higher than that of the water solution in the reactor during the entire heating shock experiment, the temperature readings of three temperature MEAs increased monotonically with time until the water solution reached thermal equilibrium with the external heater after 540 s (Fig. 6b) and heat transfer stopped. Additionally, the axial and tangential velocities were the highest at the deep location of the reactor due to the stirrer location (Aho and Karvinen, 2007), leading to the fastest rate of heat transfer. Along with this fast heat transfer, the heater directly contacted with the reactor

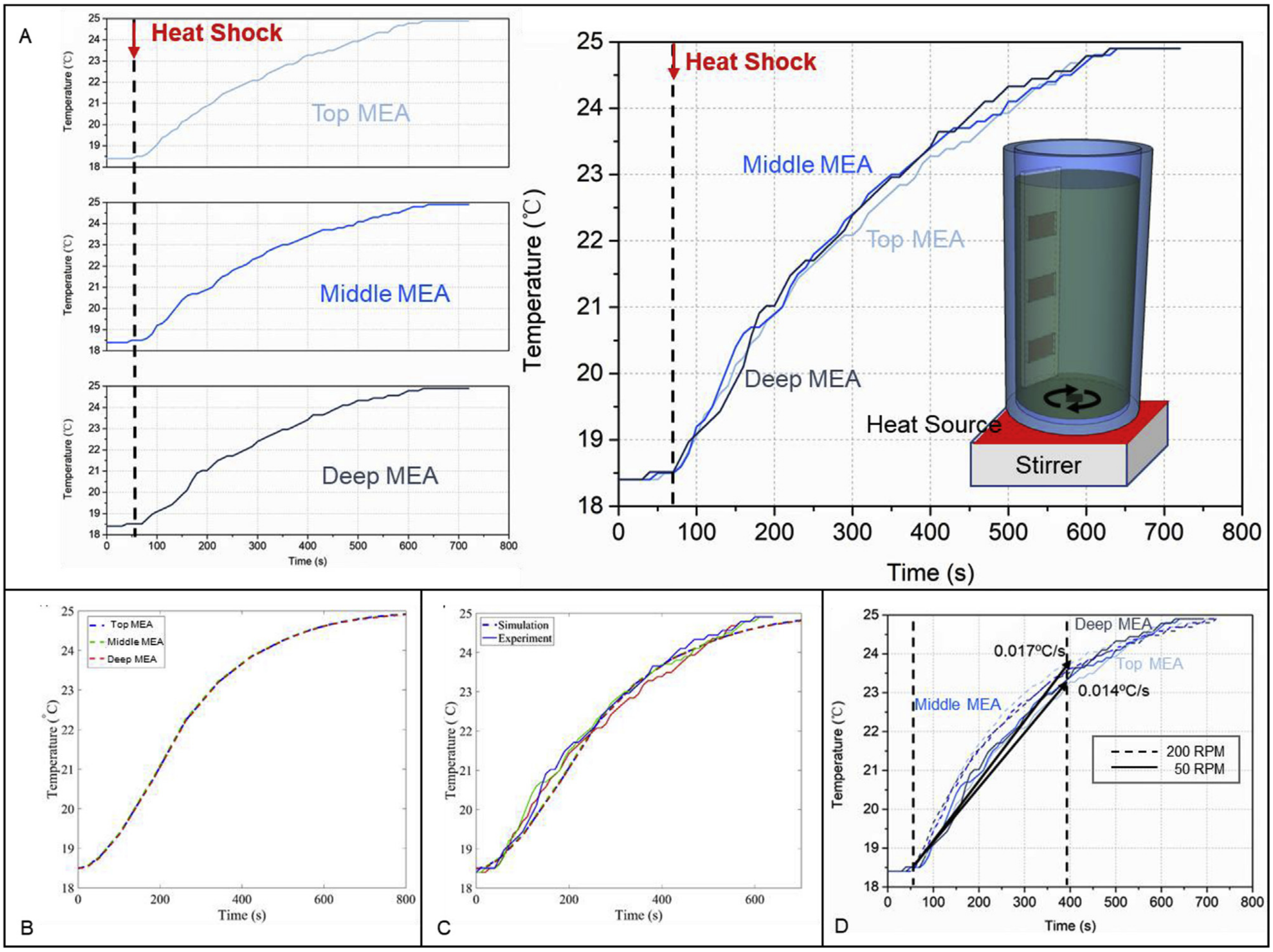

Fig. 6. Heterogeneity profiling of temperature with the heating on the deep of the reactor occurring at the 60th second. (A: Three temperature MEAs responses after the 60th second shock; B: Simulation results of temperature heterogeneity profiling for three MEAs; C: Comparison between simulation (dashed line) and experiment (solid line) of electrodes for temperature; D: The profile comparison between three temperature sensors 50 and 200 rpms.).

bottom and the length of the reactor was only 180 mm, all of which resulted in the similar temperature readings of three MEAs along the reactor depth (Fig. 6b).

3.4. *Estimation of energy/chemical dosage saving and treatment performance enhancement using Monte Carlo simulation*

Based on the experimental results obtained from the MEA profiles of three parameters, energy-saving operation through high-fidelity MEA profiling along the length of a plug-flow aerobic nitrification tank was simulated using the Monte-Carlo method (Fig. 7a). The assumptions for the parameter variation through the tank are described below. The temperature of wastewater increases along the length of the tank due to exothermic reactions carried out by microorganisms in wastewater (Hellinga et al., 1998), with the normal range of 20 °C-30 °C and the optimal temperature of 30 °C (Kim et al., 2017). The pH decreases due to nitrification reactions, with the normal range of 6.5–7 and the optimal pH of 7.0 (Ripley et al., 1986). The conductivity can be used to indicate the NH_4^+ concentration (Levlin, 2010), through which the oxygen demand can be determined (Ruiz et al., 2003). For treatment performance estimation, it was directly related with microbial activities (Rajeshwari et al., 2000), which was assumed to be 100% at water temperature of 30 °C (Wijtes et al., 1993), and drop to 15% when the temperature was down to 10 °C, and drop to 20% when the temperature up to 45 °C.

In Monte-Carlo simulation, each parameter would vary linearly in the aforementioned range through the length of the plug-flow system monitored by either “single point” sensor in a zone or multi-MEA sensors deployed in multiple zones along the system (8 zones in total in this simulation, Fig. 7a). The feedback control strategy can be executed based on the MEA profiles to make the system operate at the optimal set-point values in each zone, which is expected to enhance the system performance and save energy. For example, temperature is assumed to increase from 20 °C to 30 °C along the length of the system and follow the uniform distribution in each zone, so that the temperature would be a random number (T) between 20 and 21.25 in Zone 1 (Fig. 7a). For the existing single-point sensor (e.g., located in the Zone 1, the worst-case scenario with the lowest temperature), the temperature of the entire system would be increased by the value $\delta = 30 - \boldsymbol{T}$ to reach the optimal set-point temperature (30 °C). In contrast, the high-fidelity MEA profiling in 8 zones along the system will enable more accurate control and temperature adjustment based on the specific need in each zone rather than the whole system (Fig. 7b). The consequent energy saving was estimated to be 46.58% compared with the single-point sensor located in Zone 1 (Table S1). The chemical dosage for pH adjustment based on the single-point

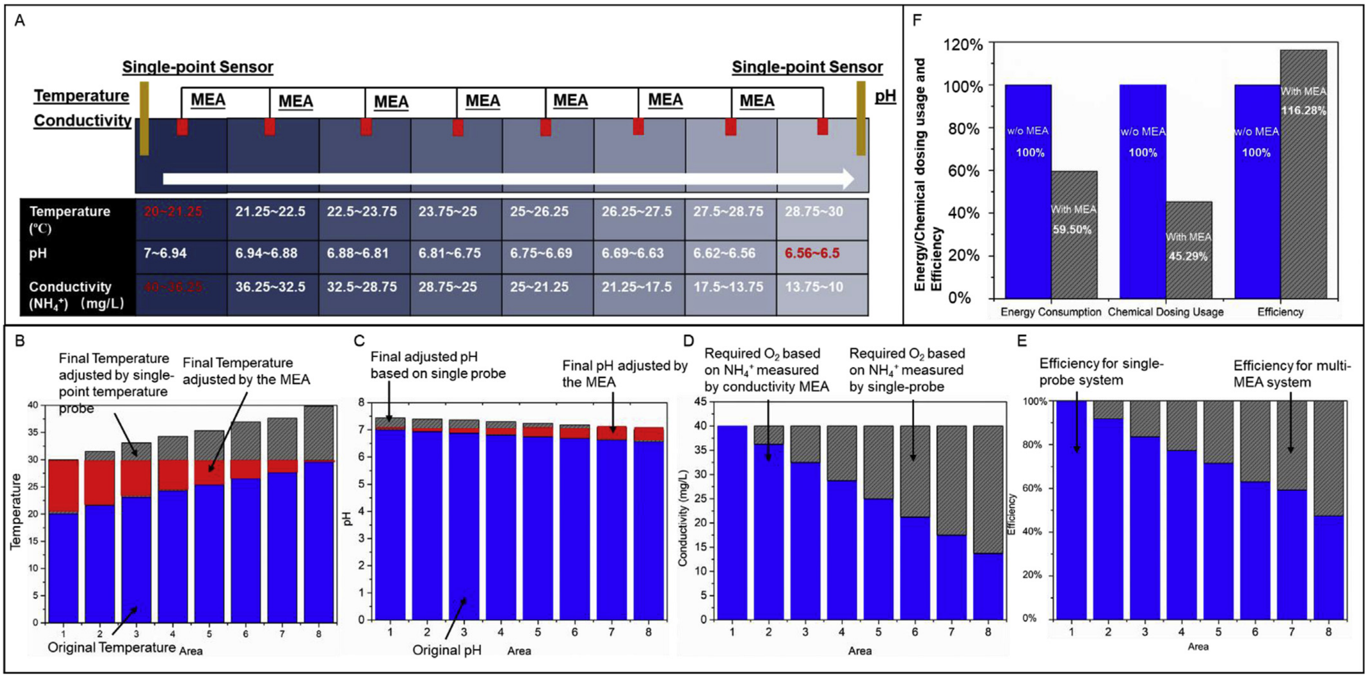

Temperature (°C)	20~21.25	21.25~22.5	22.5~23.75	23.75~25	25~26.25	26.25~27.5	27.5~28.75	28.75~30
pH	7~6.94	6.94~6.88	6.88~6.81	6.81~6.75	6.75~6.69	6.69~6.63	6.62~6.56	6.56~6.5
Conductivity (NH_4^+) (mg/L)	40~36.25	36.25~32.5	32.5~28.75	28.75~25	25~21.25	21.25~17.5	17.5~13.75	13.75~10

Fig. 7. Energy-saving and performance-enhancement using high-resolution MEA profiling predicted by the Monte Carlo simulation (A: Parameters setup in each zone of a heterogenous plug-flow reactor. A single point sensor is located in Zone 1 or Zone 8 while MEA sensors are located in each zone. The parameters obtained by the single-point probe are marked in red); B: Comparison of unselective temperature adjustment using the single-point probe and the personalized accurate adjustment in each zone using the MEA sensors; C: Comparison of pH adjustment between the single-point probe and the MEA sensors; D: Comparison of conductivity adjustment between the single-point probe and the MEA sensors; E:Comparison of performance between single-point probe and MEA sensors; F: Total energy saving, chemical dosage saving and performance enhancement using MEA sensors for temperature, pH and conductivity.). (For interpretation of the references to colour in this figure legend, the reader is referred to the Web version of this article.)

sensor was estimated based on the sensor location in Zone 8 (the worst-case scenario with the lowest pH), while the chemical dosage based on the MEA sensors was calculated along the length of the system (Fig. 7c), which was observed to save 54.71% of chemical dosage compared with the single point sensor (Table S1). The conductivity can be used as the indicator for NH_4^+ concentration in wastewater, which can indirectly reflect oxygen requirement (Levlin, 2010). The oxygen requirement controlled by the single-point conductivity sensor located in Zone 1 (the worst-case scenario with the highest NH_4^+ concentration) could lead to unnecessary over-aeration, while the conductivity MEA sensors located along the system can reflect the variation of oxygen requirement (Fig. 7d), which was observed to save 34.40% of energy consumption compared with single point sensor (Table S1).

Treatment performance of the plug-flow system was estimated at different temperatures along the system, with the assumption that bacterial activity was optimal at the temperature of 30 °C and led to the highest treatment performance, while bacterial activity dropped at low or high temperatures and lowered the treatment performance. For “single-point” sensor monitoring, it either missed the optimal temperature in the plug-flow system, or overestimated the system performance by taking the measured “single point” temperature as the optimal temperature. In contrast, multiple-MEA sensors captured the variation of temperature along the system, and could execute a customized control in each zone so that the optimal temperature for bacterial activity can be adjusted individually (Fig. 7e).

Overall, the energy consumption and chemical dosage in a plug-flow system using multi-MEA profiling in 8 zones were 59.53% and 45.27% of the system with “single-point” sensing, respectively, while the performance was 116.28% compared with those with “single-point” sensing (Fig. 7f, Table S1). However, the Monte-Carlo simulation predicted that the enhancement extent of energy-saving and treatment performance was expected to steadily drop with more MEA sensors being deployed (Fig. S5). For example, the rate of performance enhancement would drop to 0.1% when the sensor number was increased from 19 to 20. The optimized sensor deployment including sensor numbers and sensor distance should be considered in terms of monitoring performance and deployment economics. In this study, the parameters such as temperature were assumed to vary linearly along the plug-flow reactor due to biochemical reactions. The optimized sensor number can be calculated by the initial and the final concentrations (Supplementary Material: Calculation S1.1), while the sensor deployment economics should balance the trade-off between the sensor cost (e.g., capital cost and maintenance) and the system enhancement (e.g., energy-saving, chemical saving, and treatment performance) (Supplementary Material: Calculation S1.2).

3.5. *Distinct advantages of multiple MEA over traditional single-point sensors*

The flat thin mm-sized MEA sensors developed possess distinct advantages over single-point sensors, including compact structure, integration of multiple types of miniature individually addressable sensors, cost-effective mass deployment to visualize systems at high spatiotemporal resolution, and less intrusion to wastewater treatment units. By utilizing high-resolution MEA profiling in physiochemical and biochemical systems, heterogeneous status (e.g., pH and temperature variation along systems) and abnormity (e.g., influent shocks, deficient aeration, dead mixing zone) could be promptly captured, based on which efficient decision making strategies can be execute without time delay for enhanced stability and resilience. In the meantime, high-resolution MEA profiling can also validate the homogeneity incurred by complete mixing in CSTR systems, which clearly visualize systems and provide the real-time information to ensure mixing effectiveness. In contrast, traditional single-point sensors could not detect heterogeneity within the reactor under steady state and shocks nor validate homogeneity/uniformity under complete mixing.

3.6. *Significance of high-fidelity MEA profiling for energy-saving wastewater treatment*

High-resolution heterogeneity/homogeneity profiling is essential for system visualization, real-time feedback control, process analysis, and energy consumption estimation in wastewater treatment systems such as aerobic tanks, anaerobic digesters, fermenters, and disinfection contact tanks. Optimizing the performance and economics of wastewater treatment process operation relies on the ability to observe the states of the system, accurately predict transient behavior, and effectively manipulate its behavior in real-time. Due to the scale and biochemical complexity of wastewater treatment operations, there exists substantial solution heterogeneity throughout the process, posing significant challenges to the operations optimization problem as conventional systems lack the appropriate sensors to fully-observe the system, and therefore existing models can't be validated and used for real-time control. Using the high-resolution sensors discussed herein, within wastewater treatment systems, we are able to fully-characterize the heterogeneous solution characteristics and subsequently validate predictive models (e.g., the computational fluid dynamic model presented). In turn, these models and data can be used to generate and validate highly-predictive reduced-order models for nonlinear control of wastewater treatment processes.

With high fidelity and low fabrication cost, MEA sensor array fabricated using IPT has a great potential as the substitute of traditional expensive single point online sensors to offer high-resolution controllability, assure the real-time optimization of operations in a closed-loop fashion, and ultimately lead to energy-saving, high-performance, robust and dynamic processes. By targeting three typical operational parameters (conductivity, temperature and pH), this study clearly demonstrates the heterogeneity of transient shocks in systems and the enhancement of energy-savings and treatment performance using high-resolution MEA profiling.

4. Conclusions

The high-resolution sensors discussed herein enable fully-characterizing the heterogeneous solution characteristics and subsequently validate predictive models (e.g., the computational fluid dynamic model). In turn, these models and data can be used to generate and validate highly-predictive reduced-order models for nonlinear control of wastewater treatment processes. MEA profiling well captured the heterogeneity under transient shocks (conductivity and pH) and slow lingering shocks (temperature) along the reactor depth, as well as homogeneity of uniform mixing under steady state. Monte Carlo simulation estimated the energy-saving, chemical dosage saving, and treatment performance enhancement in a system with multi-MEA profiling compared with the one with traditional “single-point” sensor. This study demonstrates that MEA sensors have the immense potential to replace traditional expensive and bulky single-point sensors to enable high-resolution controllability that ensures the real-time optimization of operations in a closed-loop fashion, enhances treatment performance and enables high-resilience energy-saving wastewater treatment processes.

Acknowledgement

This study was supported by the National Science Foundation Environmental Engineering Program GOALI Project (Grant No: 1706343), NSF Partnerships for Innovation (PFI) Accelerate Innovative Research (AIR) Project (Grant No: 1640701), and Environmental Protection Agency Nitrogen Sensor Challenge Project (Grant No.: OWSEPTICSYS 171400). Yuankai Huang and Tianbao Wang are supported by the China Scholarship Council (CSC) Doctorate Program.

Appendix A. Supplementary data

Supplementary data to this article can be found online at https://doi.org/10.1016/j.watres.2019.114971.

References

Adadevoh, J.S., Ostvar, S., Wood, B., Ford, R.M., 2017. Modeling transport of chemotactic bacteria in granular media with distributed contaminant sources. Environ. Sci. Technol. 51 (24), 14192–14198.

Aho, T., Karvinen, R., 2007. In: Convection heat transfer in baffled mixing tank. HEFAT 2007.

Ahsan, S., Rahman, M.A., Kaneco, S., Katsumata, H., Suzuki, T., Ohta, K., 2005. Effect of temperature on wastewater treatment with natural and waste materials. Clean Technol. Environ. Policy 7 (3), 198–202.

Al-Ghusain, I.A., Huang, J., Hao, O.J., Lim, B.S., 1994. Using pH as a real-time control parameter for wastewater treatment and sludge digestion processes. Water Sci. Technol. 30 (4), 159–168.

Beltrá, A., Iniesta, J., Gras, L., Gallud, F., Montiel, V., Aldaz, A., Canals, A., 2003. Development of a fully automatic microwave assisted chemical oxygen demand (COD) measurement device. Instrum. Sci. Technol. 31 (3), 249–259.

Bishop, P.L., Yu, T., 1999. A microelectrode study of redox potential change in biofilms. Water Sci. Technol. 39 (7), 179.

Borja, R., Banks, C.J., 1995. Response of an anaerobic fluidized bed reactor treating ice-cream wastewater to organic, hydraulic, temperature and pH shocks. J. Biotechnol. 39 (3), 251–259.

Chang, I.-S., Le Clech, P., Jefferson, B., Judd, S., 2002. Membrane fouling in membrane bioreactors for wastewater treatment. J. Environ. Eng. 128 (11), 1018–1029.

Choi, D.-J., Park, H., 2001. A hybrid artificial neural network as a software sensor for optimal control of a wastewater treatment process. Water Res. 35 (16), 3959–3967.

De Figueiredo, M.L., Calderbank, P., 1979. The scale-up of aerated mixing vessels for specified oxygen dissolution rates. Chem. Eng. Sci. 34 (11), 1333–1338.

Dewettinck, T., Van Hege, K., Verstraete, W., 2001. The electronic nose as a rapid sensor for volatile compounds in treated domestic wastewater. Water Res. 35 (10), 2475–2483.

Dickinson, E.J., Ekström, H., Fontes, E., 2014. COMSOL Multiphysics®: finite element software for electrochemical analysis. A mini-review. Electrochem. Commun. 40, 71–74.

Duarte, F., Gormaz, R., Natesan, S., 2004. Arbitrary Lagrangian–Eulerian method for Navier–Stokes equations with moving boundaries. Comput. Methods Appl. Mech. Eng. 193 (45–47), 4819–4836.

Garcia-Ochoa, F., Gomez, E., 1998. Mass transfer coefficient in stirred tank reactors for xanthan gum solutions. Biochem. Eng. J. 1 (1), 1–10.

Ges, I.A., Ivanov, B.L., Werdich, A.A., Baudenbacher, F.J., 2007. Differential pH measurements of metabolic cellular activity in nl culture volumes using microfabricated iridium oxide electrodes. Biosens. Bioelectron. 22 (7), 1303–1310.

Grilli, F., Brambilla, R., Sirois, F., Stenvall, A., Memiaghe, S., 2013. Development of a three-dimensional finite-element model for high-temperature superconductors based on the H-formulation. Cryogenics 53, 142–147.

Hahn, C., McPeak, H., Bond, A., Clark, D., 1995. The development of new microelectrode gas sensors: an odyssey. Part 1. O2 and CO2 reduction at unshielded gold microdisc electrodes. J. Electroanal. Chem. 393 (1–2), 61–68.

Hellinga, C., Schellen, A., Mulder, J.W., van Loosdrecht, M.v., Heijnen, J., 1998. The SHARON process: an innovative method for nitrogen removal from ammonium-rich waste water. Water Sci. Technol. 37 (9), 135–142.

Huang, Y., Dehkordy, F.M., Li, Y., Emadi, S., Bagtzoglou, A., Li, B., 2018. Enhancing anaerobic fermentation performance through eccentrically stirred mixing: experimental and modeling methodology. Chem. Eng. J. 334, 1383–1391.

Hughes, T.J., Liu, W.K., Zimmermann, T.K., 1981. Lagrangian-Eulerian finite element formulation for incompressible viscous flows. Comput. Methods Appl. Mech. Eng. 29 (3), 329–349.

Ibanez, F.J., Zamborini, F.P., 2008. Chemiresistive sensing of volatile organic compounds with films of surfactant-stabilized gold and Gold– silver alloy nanoparticles. ACS Nano 2 (8), 1543–1552.

Jensen, G.C., Krause, C.E., Sotzing, G.A., Rusling, J.F., 2011. Inkjet-printed gold nanoparticle electrochemical arrays on plastic. Application to immunodetection of a cancer biomarker protein. Phys. Chem. Chem. Phys. 13 (11), 4888–4894.

Jin, B., He, Y., Shen, J., Zhuang, Z., Wang, X., Lee, F.S., 2004. Measurement of chemical oxygen demand (COD) in natural water samples by flow injection ozonation chemiluminescence (FI-CL) technique. J. Environ. Monit. 6 (8), 673–678.

Johnson, M., Andre, G., Chavarie, C., Archambault, J., 1990. Oxygen transfer rates in a mammalian cell culture bioreactor equipped with a cell-lift impeller. Biotechnol. Bioeng. 35 (1), 43–49.

Kim, M.-S., Kim, D.-H., Yun, Y.-M., 2017. Effect of operation temperature on anaerobic digestion of food waste: performance and microbial analysis. Fuel 209, 598–605.

Kinlen, P.J., Heider, J.E., Hubbard, D.E., 1994. A solid-state pH sensor based on a Nafion-coated iridium oxide indicator electrode and a polymer-based silver chloride reference electrode. Sens. Actuators B Chem. 22 (1), 13–25.

Korostynska, O., Mason, A., Al-Shamma'a, A., 2012. Monitoring of nitrates and phosphates in wastewater: current technologies and further challenges. Int. J. Smart Sens. Intell. Syst. 5 (1).

Krause, C.E., Otieno, B.A., Latus, A., Faria, R.C., Patel, V., Gutkind, J.S., Rusling, J.F., 2013. Rapid microfluidic immunoassays of cancer biomarker proteins using disposable inkjet-printed gold nanoparticle arrays. ChemistryOpen 2 (4), 141–145.

Le-Clech, P., Chen, V., Fane, T.A., 2006. Fouling in membrane bioreactors used in wastewater treatment. J. Membr. Sci. 284 (1–2), 17–53.

Lee, C.-Y., Hsieh, W.-J., Wu, G.-W., 2008. Embedded flexible micro-sensors in MEA for measuring temperature and humidity in a micro-fuel cell. J. Power Sources 181 (2), 237–243.

Lee, C.-Y., Lee, G.-B., 2003. Micromachine-based humidity sensors with integrated temperature sensors for signal drift compensation. J. Micromech. Microeng. 13 (5), 620.

Lee, J.-H., Lim, T.-S., Seo, Y., Bishop, P.L., Papautsky, I., 2007. Needle-type dissolved oxygen microelectrode array sensors for in situ measurements. Sens. Actuators B Chem. 128 (1), 179–185.

Levlin, E., 2010. Conductivity Measurements for Controlling Municipal Waste-Water Treatment.

Linsenmeier, R.A., Yancey, C.M., 1987. Improved fabrication of double-barreled recessed cathode O2 microelectrodes. J. Appl. Physiol. 63 (6), 2554–2557.

Marzouk, S.A., Ufer, S., Buck, R.P., Johnson, T.A., Dunlap, L.A., Cascio, W.E., 1998. Electrodeposited iridium oxide pH electrode for measurement of extracellular myocardial acidosis during acute ischemia. Anal. Chem. 70 (23), 5054–5061.

Massé, D.I., Masse, L., 2001. The effect of temperature on slaughterhouse wastewater treatment in anaerobic sequencing batch reactors. Bioresour. Technol. 76 (2), 91–98.

Mooney, C.Z., 1997. Monte Carlo Simulation. Sage Publications.

Nowack, B., 2003. Environmental chemistry of phosphonates. Water Res. 37 (11), 2533–2546.

Odu, S.O., Koster, P., van der Ham, A.G., van der Hoef, M.A., Kersten, S.R., 2016. Heat transfer to sub-and supercritical water flowing upward in a vertical tube at low mass fluxes: numerical analysis and experimental validation. Ind. Eng. Chem. Res. 55 (51), 13120–13131.

Ogut, A., Hatch, R.T., 1988. Oxygen transfer into Newtonian and non-Newtonian fluids in mechanically agitated vessels. Can. J. Chem. Eng. 66 (1), 79–85.

Pehlivanoglu-Mantas, E., Sedlak, D.L., 2008. Measurement of dissolved organic nitrogen forms in wastewater effluents: concentrations, size distribution and NDMA formation potential. Water Res. 42 (14), 3890–3898.

Rajeshwari, K., Balakrishnan, M., Kansal, A., Lata, K., Kishore, V., 2000. State-of-the-art of anaerobic digestion technology for industrial wastewater treatment. Renew. Sustain. Energy Rev. 4 (2), 135–156.

Ripley, L., Boyle, W., Converse, J., 1986. Improved alkalimetric monitoring for anaerobic digestion of high-strength wastes. J. Water Pollut. Control Fed. 406–411.

Ruiz, G., Jeison, D., Chamy, R., 2003. Nitrification with high nitrite accumulation for the treatment of wastewater with high ammonia concentration. Water Res. 37 (6), 1371–1377.

Schaider, L.A., Rodgers, K.M., Rudel, R.A., 2017. Review of organic wastewater compound concentrations and removal in onsite wastewater treatment systems. Environ. Sci. Technol. 51 (13), 7304–7317.

SYSTEMS, A.W.P.C., 2018. Why pH Is Important in Wastewater Treatment [WWW Document]. https://www.alarcorp.com/blog/2016/08/02/ph-important-wastewater-treatment/.

Valverde, M., Bettega, R., Badino, A., 2016. Numerical evaluation of mass transfer coefficient in stirred tank reactors with non-Newtonian fluid. Theor. Found. Chem. Eng. 50 (6), 945–958.

Wijtes, T., McClure, P., Zwietering, M., Roberts, T., 1993. Modelling bacterial growth of Listeria monocytogenes as a function of water activity, pH and temperature. Int. J. Food Microbiol. 18 (2), 139–149.

Williams, M.S., Ebel, E.D., 2014. Fitting a distribution to censored contamination data using Markov chain Monte Carlo methods and samples selected with unequal probabilities. Environ. Sci. Technol. 48 (22), 13316–13322.

Wunderlin, P., Mohn, J., Joss, A., Emmenegger, L., Siegrist, H., 2012. Mechanisms of N2O production in biological wastewater treatment under nitrifying and denitrifying conditions. Water Res. 46 (4), 1027–1037.

Xianghua, H.H.Z.J.W., Jun, G.Y.Z., 2009. Study on energy saving methods for Ã 2/O process in wastewater treatment plants [J]. Chin. J. Environ. Eng. 1, 008.

Xu, P., Zeng, G.M., Huang, D.L., Feng, C.L., Hu, S., Zhao, M.H., Lai, C., Wei, Z., Huang, C., Xie, G.X., 2012. Use of iron oxide nanomaterials in wastewater treatment: a review. Sci. Total Environ. 424, 1–10.

Xu, Z., Dong, Q., Otieno, B., Liu, Y., Williams, I., Cai, D., Li, Y., Lei, Y., Li, B., 2016. Real-time in situ sensing of multiple water quality related parameters using micro-electrode array (MEA) fabricated by inkjet-printing technology (IPT). Sens. Actuators B Chem. 237, 1108–1119.

Xu, Z., Zhou, W., Dong, Q., Li, Y., Cai, D., Lei, Y., Bagtzoglou, A., Li, B., 2017. Flat flexible thin milli-electrode array for real-time in situ water quality monitoring in distribution systems. Environ. Sci.: Water Res. Technol. 3 (5), 865–874.

Yan, B., Chen, H.Y., Luh, P.B., Wang, S., Chang, J., 2011. Optimization-based Litho Machine Scheduling with Multiple Reticles and Setups. IEEE, pp. 114–119.

Yang, L., Zeng, S., Chen, J., He, M., Yang, W., 2010. Operational energy performance assessment system of municipal wastewater treatment plants. Water Sci. Technol. 62 (6), 1361–1370.

Ylén, J.-P., 2001. Measuring, Modelling and Controlling the pH Value and the Dynamic Chemical State. Helsinki University of Technology.

Yu, H., Ma, C., Quan, X., Chen, S., Zhao, H., 2009. Flow injection analysis of chemical oxygen demand (COD) by using a boron-doped diamond (BDD) electrode. Environ. Sci. Technol. 43 (6), 1935–1939.

High-fidelity Profiling and Modeling of Heterogeneity in Wastewater Systems Using Milli-electrode Array (MEA): Toward High-Efficiency and Energy-Saving Operation

Zhiheng Xu[1], Farzaneh MahmoodPoor Dehkordy[1], Yan Li[2], Yingzheng Fan[1], Tianbao Wang[1], Yuankai Huang[1], Wangchi Zhou[1], Qiuchen Dong[3], Yu Lei[3], Matthew D. Stuber[3], Amvrossios Bagtzoglou[1], Baikun Li[1*]

[1] Department of Civil & Environmental Engineering, University of Connecticut, Storrs, Connecticut 06269, United States

[2] Department of Environmental Engineering, Jilin University, Changchun, Jilin Province, China, 130022

[3] Department of Chemical and Biomolecular Engineering, University of Connecticut, Storrs, Connecticut 06269, United States

(*corresponding author: baikun.li@uconn.edu; Phone: 860-486-2339)

Figure S1. The transient surface temperature of the heat plate during the thermal shock experiment.

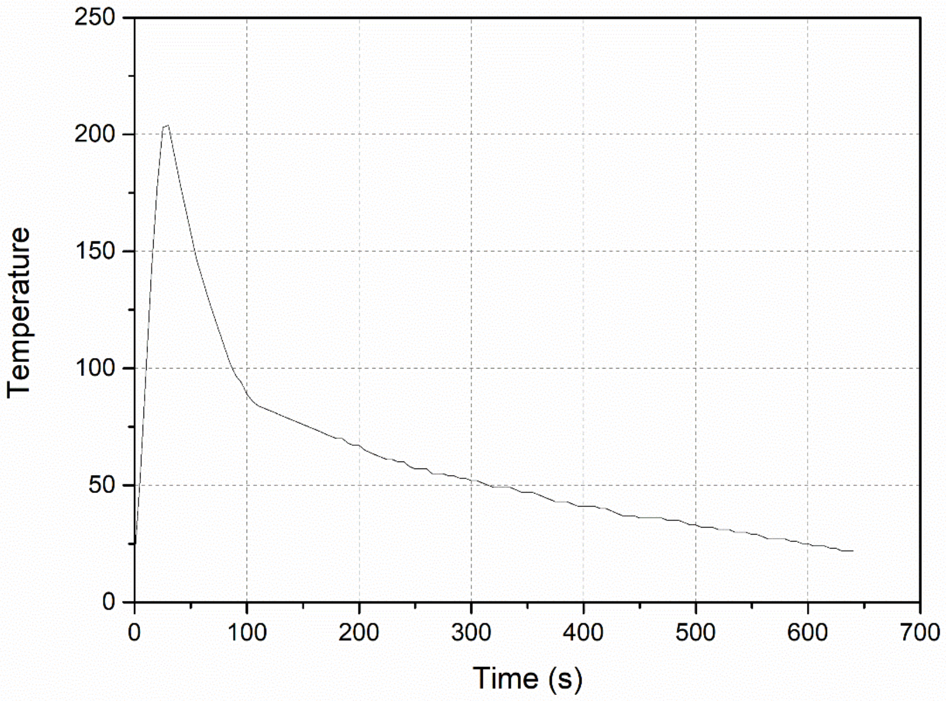

Figure S2. Comparison of mass transfer patterns of the water solution within the continuously-stirred tank reactor under conductivity (A) and pH (B) shocks.

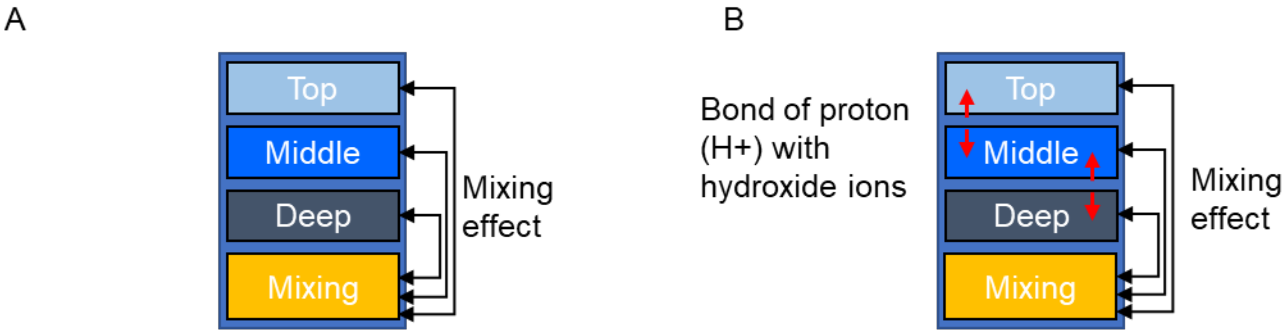

The main force of the ion diffusion is the mixing effect.

The main force of the ion diffusion is the mixing effect and the bond of proton with hydroxide ions

Figure S3. The response of the top MEA after top shock, the middle MEA to middle shock, and the deep MEA to deep shock at the conductivity shock experiments with the mixing rate of 200 RPM (A) and 50 RPM (B).

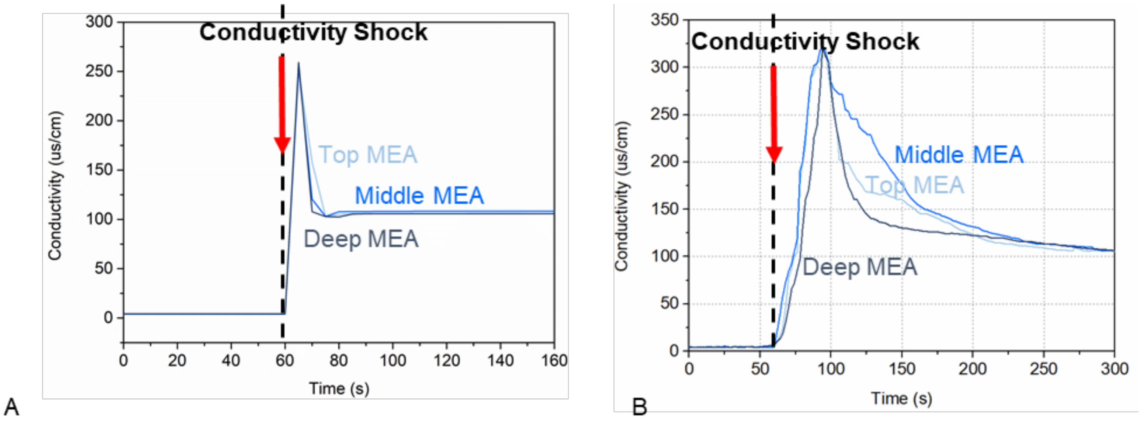

Figure S4. Results from COMSOL flow and transport simulation. The gray surface shows the reactor boundary and the three small dark blue areas indicate the locations of the sensors. (A. flow field in the reactor is shown using the streamlines. The width and color of the streamlines represent velocity magnitude; B. NaCl concentration isosurfaces for the top shock location are shown at t=95 s. The color of the isosurfaces represents the concentration of NaCl.).

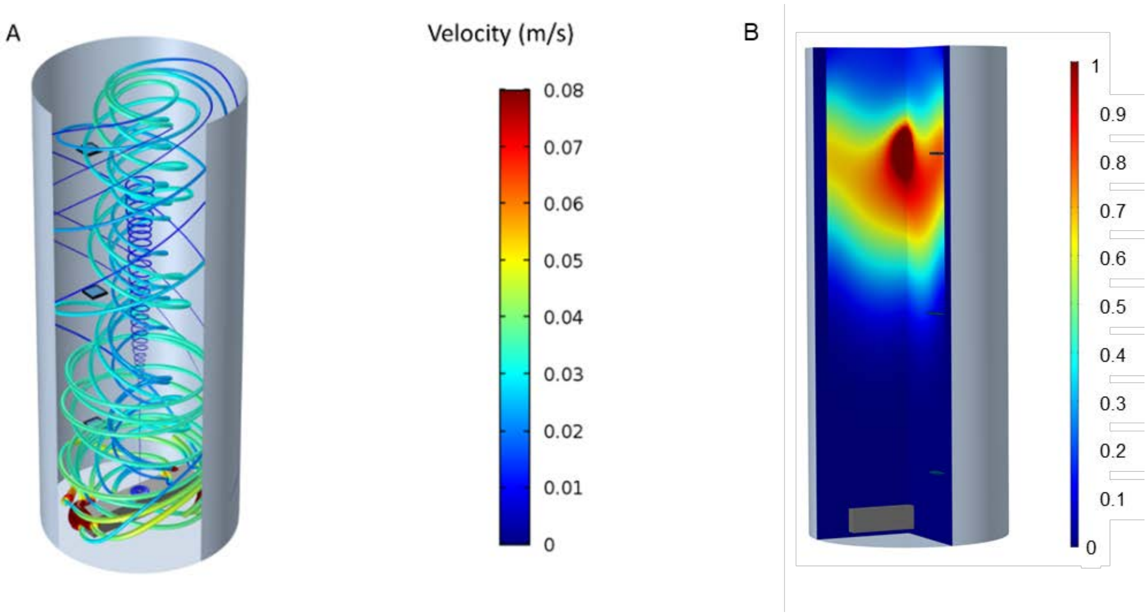

Figure S5. The variation of the enhancement extent of treatment efficiency with the sensor number (1-20) along a given system.

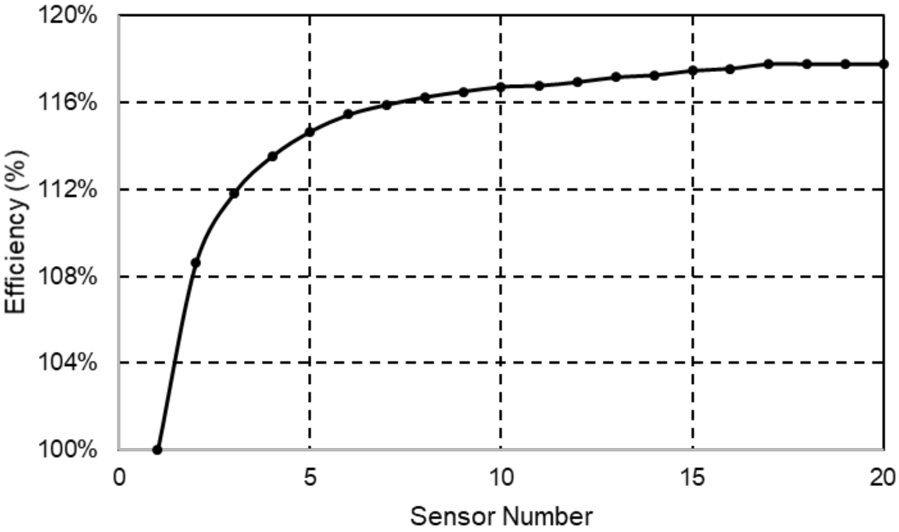

Table S1. Savings of energy and chemical dosage by MEA profiling (temperature, pH and conductivity) along the length of a plug-flow system using Monte-Carlo simulation.

Parameters (Energy Saving)	**Temperature**	**pH**	**Conductivity**	**Efficiency**
Mean	46.58%	54.71%	34.38%	86.16%
Maximum	52.25%	62.03%	39.37%	96.78%
Minimum	39.91%	47.22%	28.47%	61.39%
Median	46.66%	54.82%	34.45%	86.97%
Standard Deviation	2.04%	2.44%	1.79%	4.83%

S1.1 Monte Carlo simulation for energy consumption by 8 temperature MEA sensors

Assumption:

1. Ti is the temperature for each zone i=1,…,8.
2. T1 is the worst scenario.
3. The optimum temperature for the operation is 30 ºC.
4. C is the heat capacity of water.
5. V is the reactor volume.
6. ρ is the density of the water.
7. M is the mass of the volume, which is equal to the V*ρ.
8. The required energy calculation is based on the specific heat equation.

$$Q = CM\Delta T$$

Conclusion:

1. The required energy for the whole system using single-probe is:

   Q_S= (30-T1)CM

2. The required energy for the whole system using MEA is:

$$Q_{MEA} = \sum_{i=1}^{8} \frac{CM}{8}(30 - T_i)$$

3. Energy Saving= (Q_S-Q_{MEA})/ Q_S

S1.2 Monte Carlo simulation for treatment efficiency in a system with 8 temperature MEA sensors

Assumption:

1. Ei is the Efficiency for each zone i=1,…,8.

3. The optimum temperature for the operation is 30 ºC.

4. The efficiency for the 30 ºC is 100%

5. The efficiency would decrease with the increasing and the deceasing temperature.

6. The low temperature (10 ºC) efficiency would be 15%, and high temperature (45 ºC) efficiency would be 20%.

7. The efficiency between the high/low and the optimum temperature would linearity.

Conclusion:

1. The efficiency for the whole system using MEA is:

$$E_{MEA} = \sum_{i=1}^{8} \frac{Ei}{8}$$

S1.3 Monte Carlo simulation for chemical dosage by 8 pH MEA sensors

Assumption:

1. pHi is the pH for each zone i=1,…,8.
2. pH8 is the worst scenario.
3. The optimum pH for the operation is 7.
4. V is the reactor volume.
5. The pH adjustment is based on the base dosage, which is mass of OH^- in the calculation.
6. The pH adjustment calculation is based on the charge balance.

Conclusion:

1. The required chemical dosage for the whole system using single-probe is:

$$D_s = M_{OH^-}V(10^{-7} - pH_8)$$

2. The required energy for the whole system using MEA is:

$$D_{MEA} = \sum_{i=1}^{8} \frac{M_{OH^-}V}{8}(10^{-7} - pH_i)$$

3. Chemical Dosage Saving= $(D_S\text{-}D_{MEA})/ D_S$

S1.4 Monte Carlo simulation for energy consumption by 8 conductivity sensors

Assumption:

1. Ci (mg/L) is the conductivity each zone i=1,…,8.

2. Conductivity is the indicator of the NH_4^+ concentration.
3. C1 is the worst scenario (mg/L).
4. The calculation is based on the nitrification process.

$$2NH_4^+ + 3O_2 = 2NO_2^- + 4H^+ + 2H_2O$$

$$2NO_2^- + O_2 = 2NO_3^-$$

1 mol NH_4^+ needs 2 mol O_2 based on the reaction.

Conclusion:

1. The required oxygen for the whole system using single-probe is Es=2 M_{O2}*C1/M_{NH4+}*V
2. The required energy for the whole system using MEA is:

$$E_{MEA} = 2\sum_{i=1}^{8} \frac{M_{O_2}V}{8M_{NH_{4+}}} C_i$$

3. Energy Saving= (E_S-E_{MEA})/ E_S

S1.5 Energy/chemical dosage and efficiency usage through high-fidelity MEA profiling along the system

Assumption:

The weighting of energy usage for the temperature adjustment and aeration is 0.5 and 0.5, respectively.

Energy Usage= 1-(0.5*46.58%+0.5*34.38%) = 59.53%

Chemical Dosage Usage= 1 - Chemical Dosage Saving (pH) =45.27%

Efficiency =1/0.86=116.28%

Calculation S1

S1.6 Treatment Performance

The ideal system can get the best treatment performance by adjusting every point parameter by accurately adjusting that much what the area actual needs. The PFR reactor can be accurately approximated as several homogeneous CSTRs connected in series, with the concentration in each CSTR not varying significantly between the input and the output. In this study, we assume the concentration is stable if it changes less than 3% in each CSTR. The relationship between the concentration of the input and the output, and the CSTR dimension is shown as below.

$$(C_{input} - C_{output})v = Vr \qquad \text{Equation 1}$$

Here, C_{input} is the initial concentration, C_{output} is the final concentration, v is the volumetric flow rate, V is the volume of the small area, and r is the rate of change of concentration. The concentration of the output after n CSTRs in series is shown below.

$$(97\%\ C_0)^n = C_{final} \qquad \text{Equation 2}$$

Therefore, the number of the CSTRs (n) in series, which will be sufficiently approximate the PFR, is $\frac{\log(C_{final})}{\log(0.97C_0)}$. The length of the PFR can be calculated by using the total volume and the cross-sectional area shown below.

$$D = \frac{V}{A} \qquad \text{Equation 3}$$

Here, A is the cross-sectional area of the PFR and V is the total volume. By combining Eq.3 into Eq. 1, the PFR length is calculated below.

$$D = \frac{(C_{input}-C_{output})v}{rA} \qquad \text{Equation 4}$$

S1.2 Economic

Net present value is used in capital budgeting and investment planning to analyze the cash lows over the project lifetime. The net present value (NPV) in this study can be formulated as the following.

$$NPV = \frac{S_E - C_C - C_M}{(1+i)^1} + \sum_{k=2}^{L} \frac{S_E - C_M}{(1+i)^{k+1}} \qquad \text{Equation 5}$$

Where S_E is each year's energy saving in each year, C_C is the initial cost for the installation and other capital cost, and C_M is each year's maintenance cost, L is the project life time, and i is the discount rate. If NPV is greater than 0, it indicates the project using n sensors may be profitable. Otherwise, the project using n sensors may be rejected. S_E, C_C, C_M increases with the sensor number, so n should be determined by optimization with the economic objective, as formulated below.

$$n^* \in arg \underset{n}{max}(NPV)$$